Object motion detection enabled by reconfigurable neuromorphic vision sensor under ferroelectric modulation

Zhaoying Dang[†, ‡, ᵋ], Feng Guo[†, ‡], Zhaoqing Wang[†, ǁ], Wenjing Jie[¶], Kui Jin[ᵋ], Yang Chai[†, ǁ], Jianhua Hao[†, ‡, §, *]

[†]Department of Applied Physics, The Hong Kong Polytechnic University, Hong Kong 999077, China;

[‡]The Hong Kong Polytechnic University Shenzhen Research Institute, Shenzhen, Guangdong 518057, China;

[ᵋ]Songshan Lake Materials Laboratory, Dongguan, Guangdong 523808, China;

[ǁ]Joint Research Centre of Microelectronics, The Hong Kong Polytechnic University, Hong Kong 999077, China;

[¶]College of Chemistry and Materials Science, Sichuan Normal University, Chengdu, Sichuan 610066, China;

[§]Research Centre for Nanoscience and Nanotechnology, The Hong Kong Polytechnic University, Hong Kong 999077, China

[*]E-mail: jh.hao@polyu.edu.hk

ABSTRACT

Increasing demand for object motion detection (OMD) requires shifts of reducing redundancy, heightened power efficiency, and precise programming capabilities to ensure consistency and accuracy. Drawing inspiration from object motion sensitive ganglion cells, we propose OMD vision sensor with simple device structure of WSe_2 homojunction modulated by ferroelectric copolymer. Under optically mode and intermediate ferroelectric modulation, vision sensor can generate progressive and bidirectional photocurrents with discrete multi-states under zero power consumption. This design enables reconfigurable devices to emulate long-term potentiation and depression for synaptic weights updating, which exhibit 82 states (more than 6 bits) with uniform step of 6 pA. Such OMD devices also demonstrate non-volatility, reversibility, symmetry, and ultra-high linearity achieving a fitted R^2 of 0.999 and nonlinearity values of 0.01/-0.01. Thus, vision sensor could implement motion detection by sensing only dynamic information based on brightness difference between frames while eliminating redundant data from static scene. Additionally, neural network utilizing linear result can recognize the essential moving information with high recognition accuracy of 96.8%. We also present the scalable potential via a uniform 3×3 neuromorphic vision sensor array. Our work offers a platform to achieve motion detection based on controllable and energy-efficient ferroelectric programmability.

KEYWORDS: ferroelectricity; 2D materials; neuromorphic vision sensor; high-linear nonvolatile multi-states; object motion detection

INTRODUCTION

Static image pre-processing, encompassing noise reduction, brightness enhancement, and recognition, has been extensively demonstrated in diverse vision architectures.[1-5] In contrast, object motion detection (OMD) has emerged as a critical and burgeoning necessity across various applications, such as health monitoring, virtual reality, and intelligent transportation systems.[6, 7] Conventional motion detection architectures based on dynamic vision system separate the sensor,

memory, and computational units, resulting in substantial volumes of redundant data and high power consumption.[8, 9] The human retina possesses an inherent ability to efficiently perceive and process dynamic information at sensory stage.[10] This characteristic enables the reduction of data volume and minimizes power consumption, thereby boosting the efficiency of information processing.[11, 12]

Neuromorphic vision sensors, drawing inspiration from the biological nervous system, have been developed to replicate human visual perception.[13, 14] In the context of interference and learning applications, neural networks with high accuracy and energy efficiency play a pivotal role.[15, 16] The highly linear synaptic weights with multiple distinguishable levels and excellent symmetry greatly impact the uniformity and accuracy performance of the vision sensor system. Above features have become fundamental requirements for specialized tasks such as image recognition, autonomous driving, and virtual reality motion learning.[17] Simultaneously, enhancing overall energy efficiency and establishing self-powered systems are essential for visual sensors.[18] By reducing power requirements, devices can operate seamlessly and continuously, which is particularly valuable for long-term monitoring. Additionally, neuromorphic vision sensor exhibits potential in various portable hardware applications, in which minimizing power consumption effectively mitigates heat dissipation concerns. However, it remains a challenge to develop a vision sensor for motion detection that encompasses above advantages, including eliminating data redundancy, possessing discrete and stable multi-synaptic weights levels, and reducing power consumption. In this regard, the integration of two-dimensional (2D) materials with ferroelectrics holds promise.[19] The characteristic of ferroelectric gates, stemming from the presence of multiple intermediate levels between the fully "up" and "down" states, enables versatile regulation. This attribute facilitates precise control over doping degree and reversible electronic behaviors of atomically thin 2D materials.[20] Such approach enhances the flexibility and tunability in accurately programming neuromorphic devices to achieve ultra-linear and discrete multiple weights, offsetting the less-controllable methods and unpredictable fluctuation limitations associated with vacancy migration and ion transport mechanisms.[21-23] Especially, in the reconfigurable architecture, the diverse local switching introduces additional dimensions for optoelectronic applications. Furthermore, utilization of ferroelectric modulation provides a promising alternative for low power consumption, eliminating the need of continuous voltage stimuli, and ensuring nonvolatile property without flash storage devices.[24, 25]

Therefore, we demonstrate a reconfigurable neuromorphic device based on ambipolar tungsten di-selenide (WSe_2)[26] and a ferroelectric copolymer of poly (vinylidene fluoride-trifluoroethylene) (P(VDF-TrFE)). Opposite ferroelectric polarization from separated switching area enables the precise and nonvolatile control of the PN and NP junctions in WSe_2, bringing with opposite signs of self-powered photocurrents. After progressively programming intermediate ferroelectric states, multiple bidirectional photocurrents of more than 6 bits resolution can be used for synaptic weights updating. Notably, such synaptic update behaviors exhibit symmetricity, reversibility, high linearity ($R^2 \approx 0.999$), and uniform step (≈6 pA) between each state, all of which provide stable foundation for accurate motion detection and computation.[27] By counteracting the symmetric bidirectional photocurrents, we can simulate the object motion sensitive function of ganglion cells in the retina.[28] Furthermore, we have fabricated a uniform motion sensor array to demonstrate scalability for future large-scale integration. Subsequently, the detected motion information is accurately recognized through an artificial neural network (ANN), achieving accuracy of 96.8%. Consequently, the neuromorphic vision sensor seamlessly integrates optical sensing, energy-efficient architecture,

ultra-linear weights, and motion detection computation. Our work provides a promising solution for the advanced motion detection system.

RESULTS AND DISCUSSION

The human visual system possesses the ability to accurately perceive motion and action, enabling high-speed responses in complex and uncertain surroundings.[29] In Fig. 1(a), we illustrate the implementation of local motion detection, which relies on the intricate cellular structure of the human retina. Within the retina, bipolar cells act as integrative centers, receiving input from both upstream photoreceptor cells (rods and cones) as well as lateral amacrine cells. The amacrine cells contribute to the creation of center-surround antagonism, a contextual effect that modulates the activity of ganglion cells.[30] Notably, these ganglion cells exhibit selective response to different motion, conveying information to the visual cortex through the optic nerve. Specifically, these cells remain inactive in response to self-induced motion, such as eye movements, but display robust firing when there is motion relative to the global background (Fig. 1(b)).[31] These properties enable us to discern authentic motion from static scene, thereby increasing information analysis and computation efficiency.

Drawing inspiration from the human retina, we propose a OMD with bipolar photocurrent characteristics. Fig. 1(c) illustrates the integration of ferroelectrics and 2D materials within a neuromorphic vision sensor. By polarizing the ferroelectric gate dielectric in opposite directions through distinct pulses, the formation of PN and NP junctions is achieved under zero bias voltage with high energy efficiency. When subjected to optical illumination, self-powered positive and negative photocurrents are generated. These versatile intermediate photocurrent states enable the realization of long-term potentiation (LTP) and long-term depression (LTD) processes, exhibiting nonvolatile characteristics. Furthermore, the neuromorphic vision sensor can be fabricated into sensor arrays to facilitate large-scale integration. By leveraging inter-frame difference computations,[32] moving subjects can be detected from sequential frames based on brightness differences while eliminating the static or global part with fixed brightness (Fig. 1(d)). Thus, a single neuromorphic vision sensor transistor can perform multiple functions, including sensing optical stimuli, converting them into multi-levels electrical signals, and ultimately executing OMD processing analogous to the specialized ganglion cells.

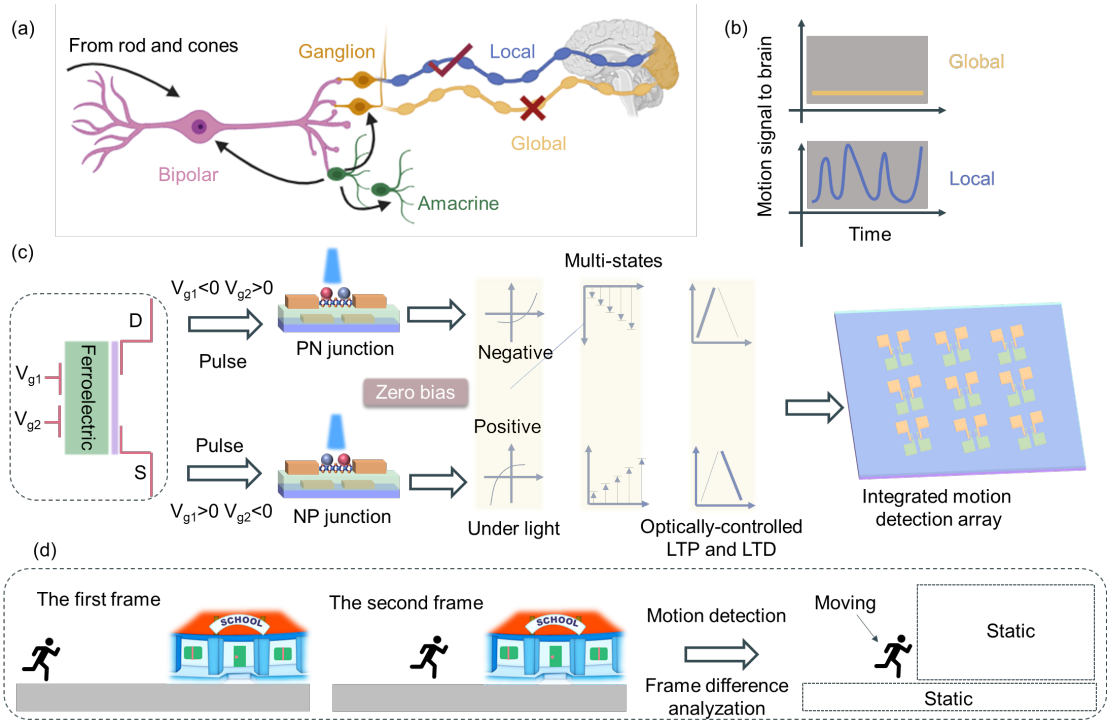

Figure 1 Neuromorphic vision sensor for OMD. (a) A schematic representation of a partial human retina, emphasizing the bipolar, amacrine, and ganglion cells while illustrating distinct responses to local and global information for motion detection (b). (c) Neuromorphic vision sensor with PN and NP configurations, facilitating the generation of nonvolatile and intermediate negative and positive photocurrents. (d) Illustration of OMD functionality, emphasizing moving object while eliminating the static information.

Reconfigurable WSe_2/P(VDF-TrFE) transistors under ferroelectric modulation

Fig. 2(a) displays a three-dimensional image of ferroelectric-modulated WSe_2 reconfigurable transistor. WSe_2 is selected as the channel due to the intrinsic ambipolar property, efficient carrier tunability, robust light-matter coupling, and effective absorption with approximate bandgap range of 1.35-1.64 eV.[33-36] These inherent characteristics contribute to the modulation of carriers within the WSe_2 channel through ferroelectric polarization. Supplementary Fig. S2 and Supplementary Fig. S3 provide the Raman spectrum and thickness of WSe_2, respectively. Moreover, the utilization of a stable organic ferroelectric material, namely P(VDF-TrFE), as the gate dielectric ensures low-temperature annealing and facilitates compatibility with the back-end-of-line regime.[37-39] The ferroelectric nature of P(VDF-TrFE) is verified through piezo-response force microscopy (PFM) methods, as depicted in Supplementary Fig. S4. The X-ray diffraction (XRD) analysis in Supplementary Fig. S5 confirms the β phase of P(VDF-TrFE), which exhibits the highest degree of ferroelectricity compared with the other phases.[40] A comprehensive understanding of the device fabrication process can be found in Method section and Supplementary Fig. S1, which provide detailed information and a flow diagram of the fabrication steps.

By employing two separated gates of Gate 1 and Gate 2, positioned beneath the P(VDF-TrFE) layer, independent ferroelectric polarization domains are formed. Fig. 2(b) illustrates the application of equal local gate voltages to induce fully polarization in the two distinct regions. In this regard, the WSe_2/P(VDF-TrFE) device serves as a typical ferroelectric field-effect transistor, exhibiting symmetric ferroelectric hysteresis. Under the polarization up (P_{up}) or down (P_{down}) states, electrons

and holes can be accumulated within the WSe_2 channel. The optical image of the device is provided in the inset of Fig. 2(b). This configuration effectively exhibits the ambipolar nature of WSe_2, as evidenced by distinct anticlockwise and clockwise hysteresis loops for the n-type and p-type branches, respectively.[41] Furthermore, the positive and negative ferroelectric switching currents (I_g) with near-equal magnitude and similar characteristics (Fig. 2(c)) serve as indicator of a small imprint field.[42] We also demonstrate the transfer characteristics and gate currents within one diagram, as shown in Supplementary Fig. S6. These findings validate the high quality of the P(VDF-TrFE) copolymers and the favorable interface between the P(VDF-TrFE) and WSe_2, thereby contributing to the enhanced photovoltaic performance.[43] In the asymmetric or unipolar mode, as illustrated in Fig. 2(d) and (e), the ferroelectric device exhibits p-type or n-type transfer curve. By fixing one gate and sweeping the other terminal, a clockwise or anticlockwise hysteresis is observed under fully P_{down} or P_{up} state, respectively. These transfer curves, obtained under different gate setting modes, provide evidence of a high on-off ratio surpassing 10^7 and a large memory window exceeding 10 V. The obtained transfer characteristics emphasize the advanced capabilities of ferroelectric-modulated WSe_2 transistor for various electronic applications such as logic circuits.[44, 45]

Furthermore, the WSe_2/P(VDF-TrFE) transistors possess four distinct output curves by defining the two gates independently, as depicted in Fig. 2(f). Specifically, when opposite gate pulses (±20 V, 1 ms) are applied to the two gates, the device exhibits characteristics of NP and PN junctions. During the reading process without external pulses, the bias voltage sweeps from -1.5 V to 1.5 V. The characteristics of output curves include rectification ratio exceeding 10^3 and an insignificant reverse current (V_{ds}=±1.5 V), which are in line with prior finding.[46, 47] Moreover, the gated regions within the WSe_2 channel can be precisely tuned to exhibit either NN or PP state with quasi-linear characteristic when both gates are set to be equal. Supplementary Fig. S7 depicts a detailed understanding of the working mechanism underlying these four configurations.

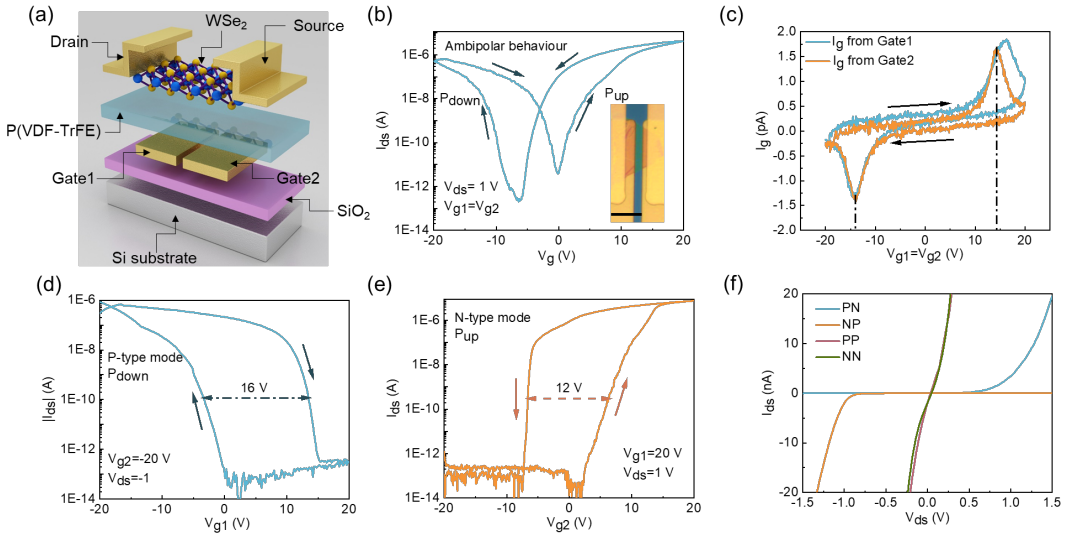

Figure 2 Reconfigurable WSe_2 devices under ferroelectric modulation. (a) A three-dimensional image of the WSe_2/P(VDF-TrFE) transistor. (b) The transfer curve under equivalent voltages of the two gates. The inset displays a real optical image of the WSe_2/P(VDF-TrFE) device, and the scale bar is 10 μm. (c) The I_g-V_g curve exhibits two separated ferroelectric switching peaks located around ±14 V with clockwise measurement direction. The ferroelectric hysteresis loops of the WSe_2/P(VDF-TrFE) device in p-type (d) and n-type (e) modes. (f) The output curves correspond to the four configurations and P(VDF-TrFE) is polarized with ±20 V gate voltage pulses.

Programmable WSe_2/P(VDF-TrFE) homojunction

Through the phase images under versatile polarization conditions, we can obtain an investigation of intermediate ferroelectric polarization states. Fig. 3(a) illustrates such process, highlighting the possibility of ferroelectric-modulated multi-states during the transition processes. P(VDF-TrFE) are fully polarized, resulting in the formation of NP state characterized by a -180° phase difference, as depicted in the PFM phase image (1) of Fig. 3(a). The P(VDF-TrFE) domains can also be manipulated to a mixed configuration with a neutral phase difference in the absence of applied voltages, depicted as (2) in Fig. 3(a). Through the gradual application of opposite voltage with NP state, ferroelectric domain undergoes a reversed switching process, as illustrated in (3)-(5) of Fig. 3(a). Eventually, a fully polarized PN junction is achieved, and phase difference becomes 180°, as exemplified in (6) of Fig. 3(a). More detailed understanding of the voltage operations and phase degree differences are shown in Supplementary Fig. S8. The results obtained from PFM analysis demonstrate that by applying opposite gate voltage pulses with the same absolute amplitudes to the two gates, the ferroelectric polarization areas can be effectively switched to reduce the original built-in electric field and reform an opposite built-in electric field. This allows for the subtle tuning of PN and NP junctions.

From an electronic standpoint, the gradual accumulation of electrons and holes occurs during the built-in field formation. The dynamic process of such phenomenon is visually represented in Fig. 3(b) and (d). During the progressive polarization process induced by the enhanced pulse amplitudes, the absolute channel current from both the PN and NP junctions exhibits a gradual increase. This behavior is clearly observed in the continuous rise of the source-drain currents extracted at V_{ds}=1.5 V (Fig. 3(c) and (e)). Remarkably, this analog current modulation behavior highlights the ability to finely manipulate the device performance. Importantly, during the read process, the gate pulses are removed due to the nonvolatile property. This nonvolatility ensures that the stored charges and the resulting current remain stable and persistent. Under the illumination of 450 nm with increasing power intensity, the PN and NP photodiodes exhibit short-circuit photocurrents (I_{sc}) (Fig. 3(f)). This photocurrent generation originates from the p-n junction and can be attributed to the photovoltaic effect.[48-50] Specifically, when the device is illuminated, the light-sensitive WSe_2 layer generates photogenerated electron-hole pairs, and these pairs are efficiently separated by the built-in electric field of the homojunctions. As a result, a self-driven I_{sc} is induced under zero bias voltage, demonstrating high power efficiency. It is noteworthy that the magnitudes of the photocurrents in the PN and NP junctions are nearly equal. Such balanced response is crucial for the functionality of OMD, and detailed discussion will be provided later. Furthermore, Fig. 3(g) suggests a linear relationship between the I_{sc} and the input power intensity for both the PN and NP photodiodes. This linear response signifies a consistent and stable photodetection performance across the examined range of light intensity. The linearity response from photodiodes makes them particularly suitable for implementation in in-sensor computing applications, as compared to phototransistors.[51]

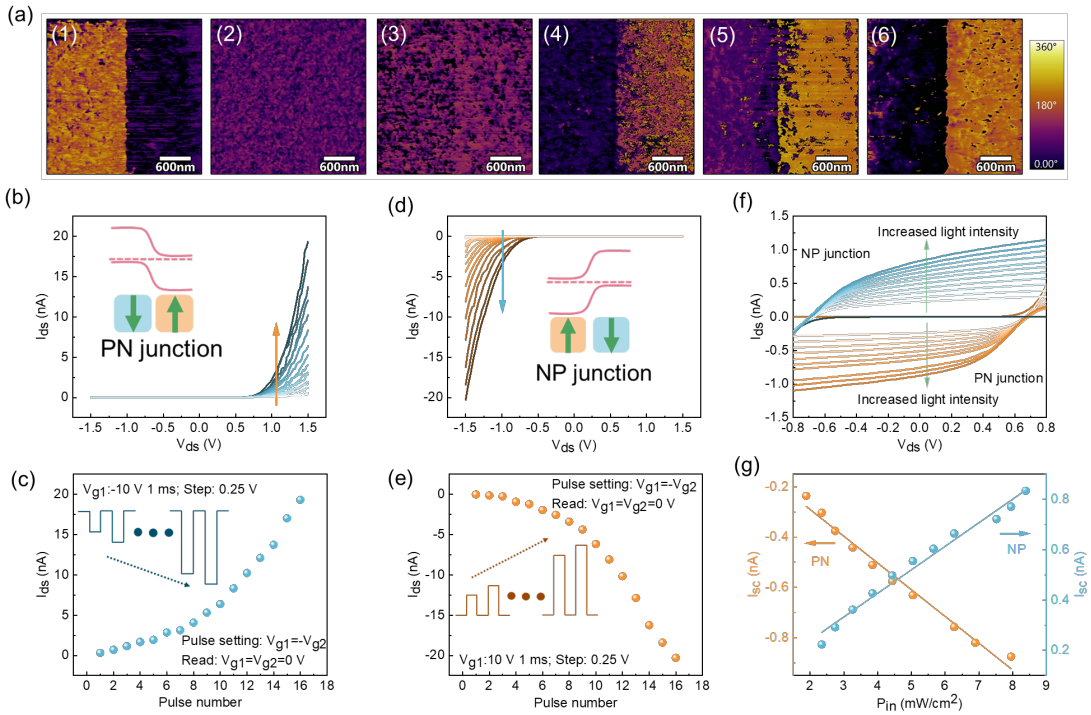

Figure 3 Programmable WSe_2/P(VDF-TrFE) homojunction. (a) PFM phase images depict the gradual transformation of homojunctions through ferroelectric polarization modulation. The output curves for PN (b) and NP (d) junctions, demonstrating the response of the devices under increased pulses magnitude. Inset: illustration of band diagram under PN and NP homojunctions. The continuous changes in source-drain currents as a function of pulses number at V_{ds}=±1.5 are illustrated for PN (c) and NP (e). The specific gate voltage conditions are initiated at 10 V and -10 V with a step of 0.25 V and then defined as zero during the read process. (f) The I_{ds}-V_{ds} curves under different input intensity for PN and NP configurations. These curves demonstrate the generation of I_{sc} under zero bias voltage. (g) The linear relationship between I_{sc} and the light intensity for PN and NP configurations.

Multiple photocurrent states of the non-volatile WSe_2/P(VDF-TrFE) transistors

The programmable and non-volatile nature of WSe_2/P(VDF-TrFE) transistors allow for the realization of intermediate photocurrent states in PN and NP junctions. Through the application of a sequence of gate voltage pulses and monitoring at a consistent light intensity, diverse positive and negative photocurrents can be attained. Taking Fig. 4(a) setting as example, a 20 V (-20 V) gate voltage pulse with 1 ms duration is initially applied to Gate1 (Gate 2), resulting in -180° phase difference and the formation of NP junction. This configuration induces positive photocurrent under illumination. Subsequently, a -10 V (10 V) gate voltage pulse with the same duration is applied to Gate1 (Gate 2) followed by gate pulses with uniform step of 0.125 V. The detailed gate voltage pulse configurations are presented in Supplementary Fig. S9. The sequence of gate voltage pulses is applied to gradually reduce the positive photocurrent, leading to a decrease in the built-in electric field of the NP junction. A similar phenomenon is observed in Fig. 4(b) when starting from the PN junction with negative photocurrent. Such reconfigurable architecture based on two separated gates provide a free and convenient platform to achieve reversible photocurrent tunability with opposite signs. The writing process involves setting the opposite voltage to Gate1 and Gate 2 without any additional bias voltage. During the reading process, only optical pulses are applied while gate and bias voltages are defined as zero due to the nonvolatility property. Fig. 4(c) and (d) offer magnified

views of the circular regions corresponding to Fig. 4(a) and (b), respectively. Notably, the positive and negative photocurrent variations demonstrate a step-like behavior, characterized by a consistently incremental or decremental change of 6 pA after each optical pulse. This uniform step pattern facilitated by precise ferroelectric programmability signifies a symmetrical and non-volatile modulation of the photocurrent, carrying potential for subsequent high-precision motion recognition tasks.[52, 53]

Through a gradual increase in the pulse number, the photocurrent undergoes a progressive transition from negative to positive values, as indicated by the blue dotted lines of Fig. 4(e). Corresponding photoresponsivity of the WSe_2 photodiode can be modulated in the same manner with dual signal values based on the relationship between photocurrent and effective light intensity (Supplementary Fig. S10). Such transition corresponds to a transformation from the initial PN to the final NP configuration, resulting in the realization of approximately 82 discrete states resolution of more than 6 bits and exceeding the capabilities of certain previous works (Supplementary Table 1). [54, 55] Conversely, by applying negative pulses onto Gate1 in conjunction with positive pulses for Gate 2, a transition from the NP to PN configuration is induced, resulting in the photocurrent returning to negative values, as depicted by the orange dotted lines. This behavior also yields 82 distinct states, indicating a highly symmetrical property. The number of states can be further enlarged by expanding the pulse range and reducing the pulse steps for higher programming capability. Importantly, both multi-level positive and negative photocurrents can be repeatedly observed, as demonstrated in cycle-2 of Fig. 4(e). This reoccurrence is made possible by the P(VDF-TrFE) ferroelectric material, which provides repeatable writing and erasing processes. The gradual ferroelectric polarization processes and corresponding band diagrams of WSe_2 are illustrated in Supplementary Fig. S11.

These multi-level of photocurrent states, characterized by bidirectional transitions, can be interpreted as LTP and LTD processes, analogous to synaptic weights in ANNs. All the progressive photocurrents exhibit linearity with R^2 coefficients of approximate 0.999 for each individual LTP and LTD processes. The nonlinearity values of 0.01/-0.01 further highlight potential for high-performance neural network computation compared to previous studies (Supplementary Table 1).[56, 57] The analysis of the nonlinearity results is presented in Supplementary Fig. S12. To provide evidence of the linearity and uniformity of the versatile LTP and LTD states in response to optical pulses, we have examined the specific synaptic processes of partial LTP and LTD within a single cycle. These detailed demonstrations are depicted in Fig. 4(f) and (g), which correspondingly illustrate the magnified views of the LTP and LTD processes in Fig. 4(e). Therefore, gradual switching of ferroelectric polarization facilitates the emulation of synaptic function and gives rise to the observed linearity for the synaptic weights updating. Above ferroelectric controlled multiple states provide stable and predictable manner for the accurate performance during the neural network training compared with other ionic migration and vacancy generation mechanism. Moreover, Fig. 4(h) demonstrates the long-term stability of 21 distinct photocurrent states encompassing positive, negative, and near-zero states, which can be extended to more states by finely tuning ferroelectric polarization through the two separated gates. These states exhibit stability over 150-second period, comparable with previous works.[58, 59] The reconfigurable WSe_2/P(VDF-TrFE) devices result in the convergence of optical signal sensing, computation, and memory storage functionalities within a single device. Such comprehensive combination enables the generation of linear, uniform, bidirectional, and multiple photocurrent responses, thereby facilitating object motion sensitive

operations that closely resemble the functioning of ganglion cells in the retina.

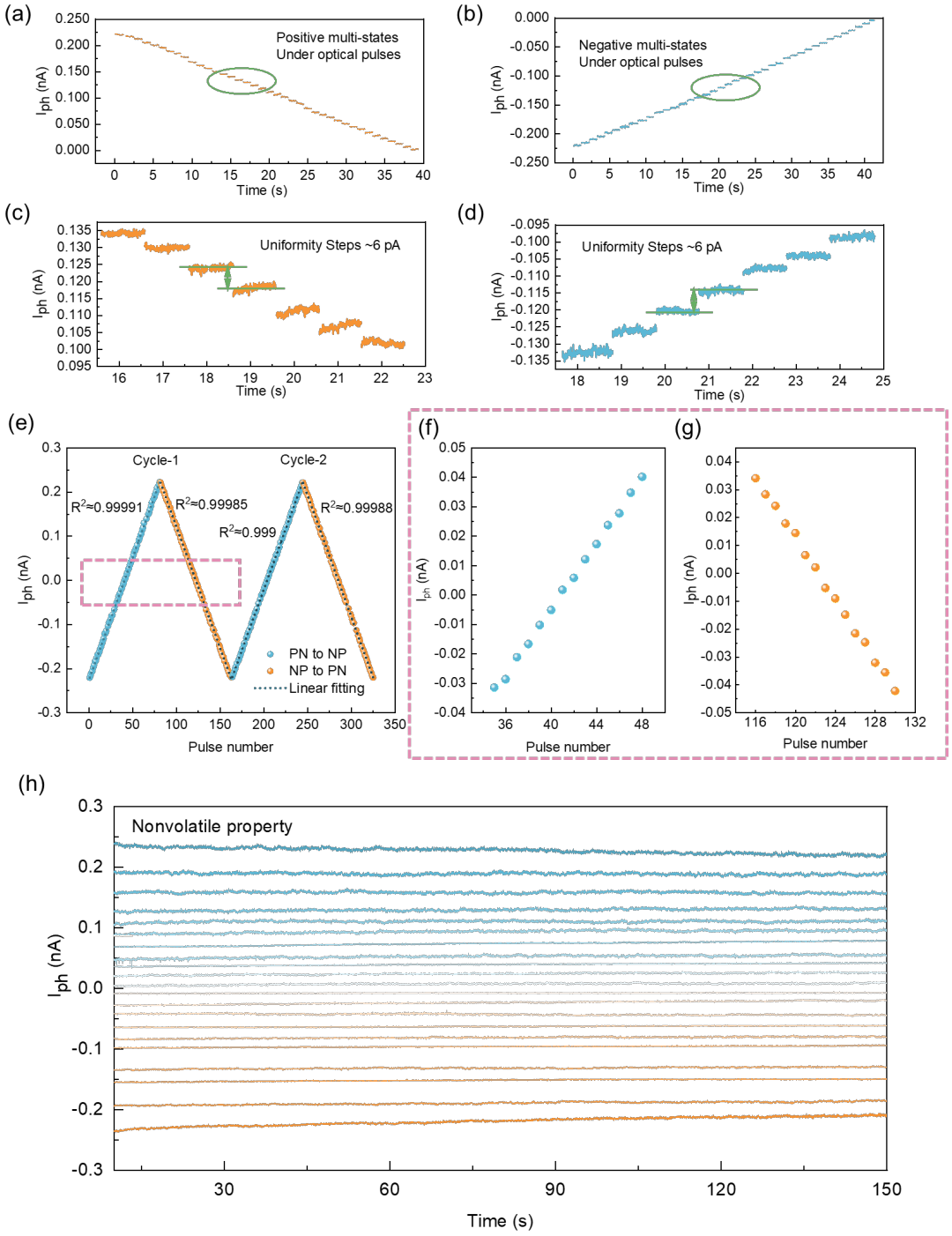

Figure 4 Multiple photocurrent states of the non-volatile WSe_2/P(VDF-TrFE) transistors. Positive (a) and negative (b) photocurrents generation when starting from NP and PN configurations, respectively. An enlarged view reveals the stable steps of multiple positive (c) and negative (d) photocurrents. These steps exhibit a uniform change of 6 pA for each optical pulse. (e) Two cycles of bidirectional LTP and LTD processes with high linearity and symmetry. Magnified view of partial LTP (f) and LTD (g) processes in cycle-1. (h) The nonvolatile property of the multiple photocurrents levels.

OMD operation based on reconfigurable WSe_2/P(VDF-TrFE) neuromorphic vision sensor

Neuromorphic vision sensor can replicate the functionality of retina in one hardware by harnessing the symmetrical and linear multi-states of bidirectional photocurrents. These devices can effectively identify and collect moving targets information from the surrounding background, mimicking the function of motion sensitive ganglion cells. Working mechanism and operation process of OMD are illustrated in Fig. 5(a). The dynamic video can be segmented into many individual frames based on the time sequence from the beginning moment t_a to the end moment t_{end}. Along with the timeline (orange dotted line), the living room is unoccupied at the initial moment t_a, providing a static global background for subsequent comparison. Within a defined interval such as from t_b to t_j, an individual enters the living room, exhibits distinct hand gestures at various moments and then leaves the room. The individual serves as a contrasting element to the original static environment. To demonstrate the moving detection results, frames at t_a and t_d are taken as examples. Each frame image is assumed to comprise M×N brightness pixels and the original brightness distribution of t_a is depicted in Fig. 5(b), with brightness values normalized between 0 and 1. On the other hand, the photocurrent states of the 2D WSe_2/P(VDF-TrFE) neuromorphic vision sensor can be assembled into positive and negative M×N photocurrent matrices, which exhibit approximately equal absolute values due to their symmetry and linearity. To perform frame difference calculations, the M×N positive and M×N negative conductance matrices are multiplied with the image brightness pixels at different moments of t_a and t_d, respectively, as indicated by the blue arrows in Fig. 5(a). The two multiplied components are then summed together to map the brightness result of the output pixels, which allows for detecting the moving person in the living room, as depicted by the pink arrows in Fig. 5(a). Such results are stored within the pixels at the corresponding moment, thanks to the nonvolatility property of the neuromorphic vision sensor. We also conduct demonstration of different hand gestures, such as waving and thumbs-up at moments t_d and t_e, respectively. The processed brightness output can effectively capture such little difference as shown in the yellow box. Within a specific period, when the background remains static and no moving objects are present, the brightness of the output pixels approaches to zero, as illustrated in Fig. 5(c). This behavior arises from the equality of absolute values between the positive and negative M×N photocurrent matrices for counteraction. By contrast, when an individual appears within a specific timeframe, the brightness pixels associated with the moving person show values above zero (Fig. 5(d) and (e)), following a normal distribution, whereas the brightness of the stationary background pixels remains zero. In Supplementary Fig. S13, we present a comprehensive analysis of the other frames (t_b, t_c, t_f, t_j) along with their processed output pixels and brightness distributions.

Moreover, we provide experimental validation of a 3×3 reconfigurable neuromorphic vision sensor array, as illustrated in Supplementary Fig. S14. Each of the nine WSe_2/P(VDF-TrFE) neuromorphic vision sensors exhibits uniformity and demonstrates bipolar electrical behaviors, as illustrated in Supplementary Fig. S15 and Supplementary S16. These findings establish a robust foundation for the advancement of scalable optical sensing and in-sensor computing applications. Furthermore, the vital information pertaining to the moving object is inputted into an ANN, as depicted in Fig. 5(f), leveraging the high-linear LTP and LTD behaviors of WSe_2/P(VDF-TrFE). For simulation purposes, we utilize the Modified National Institute of Standards and Technology (MNIST) handwritten digits dataset and a three-layer network.[60] The accuracy over 40 epochs is depicted in Fig. 5(g). During the initial epochs, the recognition accuracy experiences significant improvement and reaches a peak value of 96.8%. The high accuracy rate stems from the linear, symmetric, and distinguishable weight updating based on controllable ferroelectric polarization.

Consequently, the WSe_2/P(VDF-TrFE) neuromorphic vision sensor demonstrates the OMD process, akin to certain ganglion cells and this bionic approach reduces the generation and transmission of redundant data by emphasizing moving objects through an energy-efficient pre-processing platform.

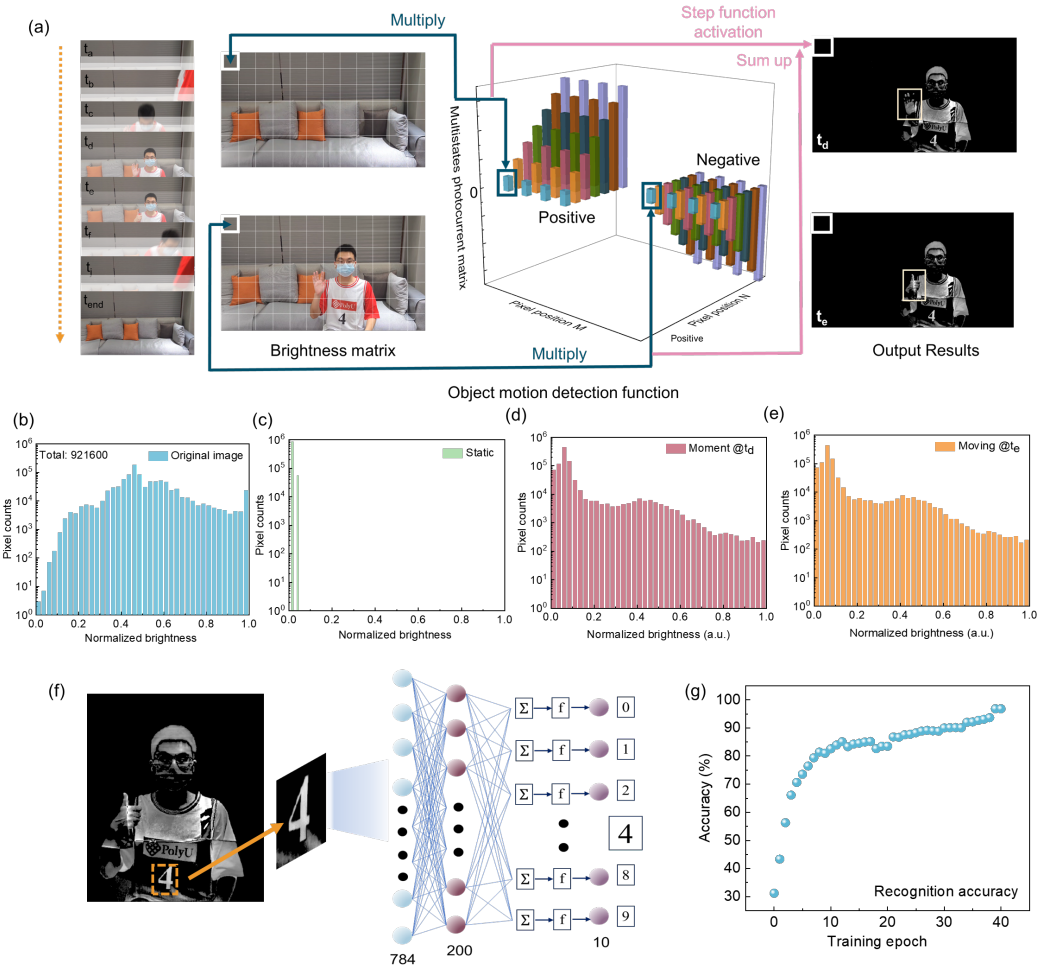

Figure 5: OMD operation based on reconfigurable WSe_2/P(VDF-TrFE) neuromorphic vision sensor. (a) The brightness pixels at different frame moments (e.g., t_a and t_d) are multiplied by the corresponding positive and negative photocurrent matrices. The resulting products are then summed to detect dynamic objects. (b) The brightness distribution in the original image, consisting of 921,600 pixels. After motion detection, output brightness distribution of static image (c), dynamic image at t_d (d), and dynamic image at t_e (e). (f) Recognition of dynamic target through neural network. (g) Accuracy results of the recognition over 40 epochs, demonstrating the high accuracy of 96.8% during training.

CONCLUSION

We have employed a reconfigurable 2D WSe_2/P(VDF-TrFE) neuromorphic vision sensor with a straightforward device structure and convenient construction strategy for motion detection. High-precision programming ability is important for moving information processing. Previous fluctuations in each state without distinguishable and uniform step have hindered various neuromorphic applications. Our neuromorphic vision sensor demonstrates programmable tunability through progressive ferroelectric polarization, enabling the generation of self-powered bidirectional photocurrents with more than 6 bits and uniform step of 6 pA. These photocurrents possess desirable properties such as nonvolatility, symmetricity, reversibility, and high linearity (R^2=0.999). We have

achieved efficient motion detection by collecting information solely from the moving object while minimizing redundant data through the bidirectional photocurrent states, like the ganglion cells in the human retina. Additionally, the constructed ANN recognize the essential moving information with accuracy 96.8%. The integration of optical signal sensing, multi-states memorization, and power-efficient modulation capabilities in the neuromorphic vision sensor holds significant promise for other artificial vision hardware. We also demonstrate a 3×3 neuromorphic vision sensor array for scalable application. It is a well-established fact that the proposed bionic vision sensor is still in its nascent stage concerning hyper-vision and practical applications such as autonomous driving, primarily due to the limitations of larger scale integration. Moreover, as representative ferroelectric copolymer with features of soft, light, and simple fabrication process, the P(VDF-TrFE) can be used for high-performance flexible electronics devices. The ferroelectric/semiconductor heterostructures with flexible property can be integrally transferred onto arbitrary substrates for advanced wearable electronics.[61] Exploring the self-powered and reconfigurable vision sensor chips along with integrated and flexible hardware holds significant potential for development of intelligent vision systems.

METHODS

Device fabrication: Initially, SiO_2/Si substrates covered by photoresist undergo the ultraviolet photolithography process to pre-pattern two split gates of 2 μm gap. Subsequently, 10 nm Cr/50 nm Au electrodes are deposited onto the substrates using thermal evaporation, followed by a lift-off process in acetone solution. The dielectric layers of P(VDF-TrFE) (70:30 in mol %) thin films are formed through spin-coating with thickness of 300 nm. These layers are then annealed at 135 ℃ for four hours. Few-layered WSe_2 flakes are obtained by mechanically exfoliating from a bulk single crystal (purchased from HQ Graphene). Desired WSe_2 flakes are identified on a PDMS substrate and transferred onto the surface of the P(VDF-TrFE) layers using a 2D Transfer system. Finally, a pair electrodes of 50 nm Au with 6 μm gap, serving as the source and drain electrodes, are transferred and aligned onto the WSe_2 channel. For a detailed illustration of the device fabrication process, please refer to Supplementary Fig. S1.

Characterization methods: The thicknesses of few-layer WSe_2 films are examined using a commercial atomic force microscope (Cypher S/Oxford Instruments Asylum Research). PFM measurements are conducted in DART PFM mode. Raman investigations of WSe_2 flakes are carried out using high-resolution confocal μ-Raman microscopes (WITEC alpha300 R) equipped with 532 nm laser sources. The WSe_2/P(VDF-TrFE) samples are tested using a semiconductor analyzer (Keysight B1500A) in a probe station (Lake Shore CRX-6.5K) under vacuum and room-temperature conditions. Gate pulses are applied using a high voltage semiconductor pulse generator unit (SPGU). For optical mode measurements, 450 nm monochromatic LED lights are used as the light source. The light intensity is calibrated using a power meter (SANWA, LP1). To perform time-dependent optical response measurements, the LED frequency is modulated using a signal function generator.

Simulation operation: Six steps are employed to perform motion detection by utilizing inter-frame differential computation and image recognition of moving objects based on the motion detection results. (1) Neuromorphic vision sensor is developed to experimentally capture positive and negative response parameters using non-volatile photocurrents; (2) Multiple frames consisting of M×N pixels are acquired from a motion process, treating it as a continuous stream of images; (3) M×N positive (W^+) and negative (W^-) weight matrices are constructed based on the response

parameters obtained in Step 1. These weight matrices are then applied to multiply the pixel values of different frames. For instance, the M×N pixels of frame $t_0(P_{t0})$ and $t_1(P_{t1})$ are multiplied by the positive and negative weight matrices W^+P_{t0} at t_0 and W^-P_{t1} at t_1, respectively; (4) The results obtained in Step 3 are summed to obtain the transformed pixel outcome, such as $W^+P_{t0} + W^-P_{t1}$. A step function is subsequently utilized to enhance the differentiation of the accumulated data. (5) The processed data is transformed into a fresh image stream utilizing OpenCV, a widely used open-source computer vision library renowned for its capabilities in image and video processing tasks; (6) Finally, an ANN is employed in conjunction with a corresponding training database to recognize the moving objects detected in Step 5. For instance, in this study, number recognition is performed by employing the PyTorch platform based on the MNIST database. Detailed flow chart of above operation is illustrated in Supplementary Fig. S17.

ASSOCIATE CONTENT

The Supporting Information is available

The thickness and Raman characterization of WSe_2, PFM measurement of P(VDF-TrFE) films, evolution of band alignment diagrams, PFM phase change under different gate voltage operations, uniformity evidence of the vison sensor array, and flow chart of inter-frame differential computation.

Author contribution

The idea was conceived by J.H and Z.D. Z.D. designed and conducted experiments. F.G. provided support for the electrical measurement. Z.W. assisted with the simulation discussion. Z.D. wrote the manuscript, and all authors contributed to the revision of the paper. J.H supervised the project.

Notes

The authors declare no competing financial interest.

ACKNOWLEDGMENTS

This work was supported by a grant from the National Natural Science Foundation of China (No. 52233014), a fellowship award from the Research Grants Council of Hong Kong (Project No. PolyU SRFS2122-5S02), AoE/P-701/20, and PolyU international grants (1-W22S and 1-CE0H).

REFERENCES

(1) Zhou, F.; Chai, Y. Near-Sensor and in-Sensor Computing. *Nat. Electron.* **2020**, *3*, 664-671.

(2) Huang, P.-Y.; Jiang, B.-Y.; Chen, H.-J.; Xu, J.-Y.; Wang, K.; Zhu, C.-Y.; Hu, X.-Y.; Li, D.; Zhen, L.; Zhou, F.-C. Neuro-Inspired Optical Sensor Array for High-Accuracy Static Image Recognition and Dynamic Trace Extraction. *Nat. Commun.* **2023**, *14*, 6736.

(3) Yu, R.; He, L.; Gao, C.; Zhang, X.; Li, E.; Guo, T.; Li, W.; Chen, H. Programmable Ferroelectric Bionic Vision Hardware with Selective Attention for High-Precision Image Classification. *Nat. Commun.* **2022**, *13*, 7019.

(4) Fu, X.; Li, T.; Cai, B.; Miao, J.; Panin, G. N.; Ma, X.; Wang, J.; Jiang, X.; Li, Q.; Dong, Y. Graphene/$MoS_{2-x}O_x$/Graphene Photomemristor with Tunable Non-Volatile Responsivities for Neuromorphic Vision Processing. *Light: Science & Applications* **2023**, *12*, 39.

(5) Dang, Z.; Guo, F.; Zhao, Y.; Jin, K.; Jie, W.; Hao, J. Ferroelectric Modulation of ReS_2-Based Multifunctional Optoelectronic Neuromorphic Devices for Wavelength-Selective Artificial Visual System. *Adv. Funct. Mater.* **2024**, 2400105.

(6) Cutler, R.; Davis, L. S. Robust Real-Time Periodic Motion Detection, Analysis, and Applications. *IEEE Transactions on pattern analysis and machine intelligence* **2000**, *22*, 781-796.

(7) Huang, S.-C. An Advanced Motion Detection Algorithm with Video Quality Analysis for Video Surveillance Systems. *IEEE transactions on circuits and systems for video technology* **2010**, *21*, 1-

14.
(8) Chai, Y. In-Sensor Computing for Machine Vision. Nature Publishing Group UK London: 2020.
(9) Wu, G.; Zhang, X.; Feng, G.; Wang, J.; Zhou, K.; Zeng, J.; Dong, D.; Zhu, F.; Yang, C.; Zhao, X. Ferroelectric-Defined Reconfigurable Homojunctions for in-Memory Sensing and Computing. *Nat. Mater.* **2023**, *22*, 1499-1506.
(10) Gollisch, T.; Meister, M. Eye Smarter Than Scientists Believed: Neural Computations in Circuits of the Retina. *Neuron* **2010**, *65*, 150-164.
(11) Masland, R. H. The Neuronal Organization of the Retina. *Neuron* **2012**, *76*, 266-280.
(12) Zhou, Y.; Fu, J.; Chen, Z.; Zhuge, F.; Wang, Y.; Yan, J.; Ma, S.; Xu, L.; Yuan, H.; Chan, M. Computational Event-Driven Vision Sensors for in-Sensor Spiking Neural Networks. *Nat. Electron.* **2023**, *6*, 870-878.
(13) Wang, Z.; Wan, T.; Ma, S.; Chai, Y. Multidimensional Vision Sensors for Information Processing. *Nat. Nanotechnol.* **2024**, *19*, 919-930.
(14) Yang, J.; Cai, Y.; Wang, F.; Li, S.; Zhan, X.; Xu, K.; He, J.; Wang, Z. A Reconfigurable Bipolar Image Sensor for High-Efficiency Dynamic Vision Recognition. *Nano Lett.* **2024**, *24*, 5862-5869.
(15) Kumar, S.; Wang, X.; Strachan, J. P.; Yang, Y.; Lu, W. D. Dynamical Memristors for Higher-Complexity Neuromorphic Computing. *Nat. Rev. Mater.* **2022**, *7*, 575-591.
(16) Luo, Z.-D.; Zhang, S.; Liu, Y.; Zhang, D.; Gan, X.; Seidel, J.; Liu, Y.; Han, G.; Alexe, M.; Hao, Y. Dual-Ferroelectric-Coupling-Engineered Two-Dimensional Transistors for Multifunctional in-Memory Computing. *ACS Nano* **2022**, *16*, 3362-3372.
(17) Yang, S. T.; Li, X. Y.; Yu, T. L.; Wang, J.; Fang, H.; Nie, F.; He, B.; Zhao, L.; Lu, W. M.; Yan, S. S.; et al. High-Performance Neuromorphic Computing Based on Ferroelectric Synapses with Excellent Conductance Linearity and Symmetry. *Adv. Funct. Mater.* **2022**, *32*, 2202366.
(18) Yang, J. J.; Grollier, J.; Williams, R. S.; Huang, R. Neuromorphic Engineering: From Materials to Device Application. *Adv. Mater.* **2023**, *35*, 2305078.
(19) Wang, C.-Y.; Liang, S.-J.; Wang, S.; Wang, P.; Li, Z. a.; Wang, Z.; Gao, A.; Pan, C.; Liu, C.; Liu, J. Gate-Tunable Van Der Waals Heterostructure for Reconfigurable Neural Network Vision Sensor. *Sci. Adv.* **2020**, *6*, eaba6173.
(20) Chen, C.; Zhou, Y.; Tong, L.; Pang, Y.; Xu, J. Emerging 2D Ferroelectric Devices for in-Sensor and in-Memory Computing. *Adv. Mater.* **2024**, 2400332.
(21) Li, Y.; Chen, S.; Yu, Z.; Li, S.; Xiong, Y.; Pam, M. E.; Zhang, Y. W.; Ang, K. W. In-Memory Computing Using Memristor Arrays with Ultrathin 2D $PdSeO_x/PdSe_2$ Heterostructure. *Adv. Mater.* **2022**, *34*, 2201488.
(22) Sun, Y.; Zhang, R.; Teng, C.; Tan, J.; Zhang, Z.; Li, S.; Wang, J.; Zhao, S.; Chen, W.; Liu, B. Internal Ion Transport in Ionic 2D $CuInP_2S_6$ Enabling Multi-State Neuromorphic Computing with Low Operation Current. *Mater. Today* **2023**, *66*, 9-16.
(23) Li, T.; Miao, J.; Fu, X.; Song, B.; Cai, B.; Ge, X.; Zhou, X.; Zhou, P.; Wang, X.; Jariwala, D. Reconfigurable, Non-Volatile Neuromorphic Photovoltaics. *Nat. Nanotechnol.* **2023**, *18*, 1303-1310.
(24) Wu, G.; Wang, X.; Chen, Y.; Wu, S.; Wu, B.; Jiang, Y.; Shen, H.; Lin, T.; Liu, Q.; Wang, X. $MoTe_2$ P–N Homojunctions Defined by Ferroelectric Polarization. *Adv. Mater.* **2020**, *32*, 1907937.
(25) Zhu, Y.; Wang, Y.; Pang, X.; Jiang, Y.; Liu, X.; Li, Q.; Wang, Z.; Liu, C.; Hu, W.; Zhou, P. Non-Volatile 2D MoS_2/Black Phosphorus Heterojunction Photodiodes in the near-to Mid-Infrared Region. *Nat. Commun.* **2024**, *15*, 6015.
(26) Lv, L.; Zhuge, F.; Xie, F.; Xiong, X.; Zhang, Q.; Zhang, N.; Huang, Y.; Zhai, T. Reconfigurable

Two-Dimensional Optoelectronic Devices Enabled by Local Ferroelectric Polarization. *Nat. Commun.* **2019**, *10*, 3331.
(27) Sun, X.; Zhu, C.; Yi, J.; Xiang, L.; Ma, C.; Liu, H.; Zheng, B.; Liu, Y.; You, W.; Zhang, W. Reconfigurable Logic-in-Memory Architectures Based on a Two-Dimensional Van Der Waals Heterostructure Device. *Nat. Electron.* **2022**, *5*, 752-760.
(28) Zhang, Z.; Wang, S.; Liu, C.; Xie, R.; Hu, W.; Zhou, P. All-in-One Two-Dimensional Retinomorphic Hardware Device for Motion Detection and Recognition. *Nat. Nanotechnol.* **2022**, *17*, 27-32.
(29) Jayachandran, D.; Oberoi, A.; Sebastian, A.; Choudhury, T. H.; Shankar, B.; Redwing, J. M.; Das, S. A Low-Power Biomimetic Collision Detector Based on an in-Memory Molybdenum Disulfide Photodetector. *Nat. Electron.* **2020**, *3*, 646-655.
(30) Ölveczky, B. P.; Baccus, S. A.; Meister, M. Segregation of Object and Background Motion in the Retina. *Nature* **2003**, *423*, 401-408.
(31) Masland, R. H. The Retina's Fancy Tricks. *Nature* **2003**, *423*, 387-388.
(32) Weng, M.; Huang, G.; Da, X. A New Interframe Difference Algorithm for Moving Target Detection. In *2010 3rd international congress on image and signal processing*, 2010; IEEE: Vol. 1, pp 285-289.
(33) Das, S.; Appenzeller, J. WSe_2 Field Effect Transistors with Enhanced Ambipolar Characteristics. *Appl. Phys. Lett.* **2013**, *103*, 103501.
(34) Qiu, H.; Liu, Z.; Yao, Y.; Herder, M.; Hecht, S.; Samorì, P. Simultaneous Optical Tuning of Hole and Electron Transport in Ambipolar WSe_2 Interfaced with a Bicomponent Photochromic Layer: From High-Mobility Transistors to Flexible Multilevel Memories. *Adv. Mater.* **2020**, *32*, 1907903.
(35) Qiu, H.; Yu, Z.; Zhao, T.; Zhang, Q.; Xu, M.; Li, P.; Li, T.; Bao, W.; Chai, Y.; Chen, S. Two-Dimensional Materials for Future Information Technology: Status and Prospects. *Science China Information Sciences* **2024**, *67*, 1-147.
(36) Zhou, C.; Zhao, Y.; Raju, S.; Wang, Y.; Lin, Z.; Chan, M.; Chai, Y. Carrier Type Control of WSe_2 Field-Effect Transistors by Thickness Modulation and MoO_3 Layer Doping. *Adv. Funct. Mater.* **2016**, *26*, 4223-4230.
(37) Luo, Z. D.; Yang, M. M.; Liu, Y.; Alexe, M. Emerging Opportunities for 2D Semiconductor/Ferroelectric Transistor-Structure Devices. *Adv. Mater.* **2021**, *33*, 2005620.
(38) Majumdar, S. Back-End Cmos Compatible and Flexible Ferroelectric Memories for Neuromorphic Computing and Adaptive Sensing. *Advanced Intelligent Systems* **2022**, *4*, 2100175.
(39) Dang, Z.; Guo, F.; Wu, Z.; Jin, K.; Hao, J. Interface Engineering and Device Applications of 2D Ultrathin Film/Ferroelectric Copolymer P (VDF-TrFE). *Advanced Physics Research* **2023**, *2*, 2200038.
(40) Sun, X.; Chen, Y.; Zhao, D.; Taniguchi, T.; Watanabe, K.; Wang, J.; Xue, J. Measuring Band Modulation of MoS_2 with Ferroelectric Gates. *Nano Lett.* **2023**, *23*, 2114-2120.
(41) Ram, A.; Maity, K.; Marchand, C.; Mahmoudi, A.; Kshirsagar, A. R.; Soliman, M.; Taniguchi, T.; Watanabe, K.; Doudin, B.; Ouerghi, A. Reconfigurable Multifunctional Van Der Waals Ferroelectric Devices and Logic Circuits. *ACS Nano* **2023**, *17*, 21865-21877.
(42) Cui, B.; Fan, Z.; Li, W.; Chen, Y.; Dong, S.; Tan, Z.; Cheng, S.; Tian, B.; Tao, R.; Tian, G. Ferroelectric Photosensor Network: An Advanced Hardware Solution to Real-Time Machine Vision. *Nat. Commun.* **2022**, *13*, 1707.

(43) Tan, Z.; Tian, J.; Fan, Z.; Lu, Z.; Zhang, L.; Zheng, D.; Wang, Y.; Chen, D.; Qin, M.; Zeng, M. Polarization Imprint Effects on the Photovoltaic Effect in Pb (Zr, Ti) O_3 Thin Films. *Appl. Phys. Lett.* **2018**, *112*, 152905.
(44) Liu, X.; Choi, M. S.; Hwang, E.; Yoo, W. J.; Sun, J. Fermi Level Pinning Dependent 2D Semiconductor Devices: Challenges and Prospects. *Adv. Mater.* **2022**, *34*, 2108425.
(45) Avsar, A.; Marinov, K.; Marin, E. G.; Iannaccone, G.; Watanabe, K.; Taniguchi, T.; Fiori, G.; Kis, A. Reconfigurable Diodes Based on Vertical WSe_2 Transistors with Van Der Waals Bonded Contacts. *Adv. Mater.* **2018**, *30*, 1707200.
(46) Pan, C.; Wang, C.-Y.; Liang, S.-J.; Wang, Y.; Cao, T.; Wang, P.; Wang, C.; Wang, S.; Cheng, B.; Gao, A. Reconfigurable Logic and Neuromorphic Circuits Based on Electrically Tunable Two-Dimensional Homojunctions. *Nat. Electron.* **2020**, *3*, 383-390.
(47) Zhou, Y.; Tong, L.; Chen, Z.; Tao, L.; Pang, Y.; Xu, J.-B. Contact-Engineered Reconfigurable Two-Dimensional Schottky Junction Field-Effect Transistor with Low Leakage Currents. *Nat. Commun.* **2023**, *14*, 4270.
(48) Dong, Y.; Yang, M.-M.; Yoshii, M.; Matsuoka, S.; Kitamura, S.; Hasegawa, T.; Ogawa, N.; Morimoto, T.; Ideue, T.; Iwasa, Y. Giant Bulk Piezophotovoltaic Effect in 3R-MoS_2. *Nat. Nanotechnol.* **2023**, *18*, 36-41.
(49) Liang, Z.; Zhou, X.; Zhang, L.; Yu, X.-L.; Lv, Y.; Song, X.; Zhou, Y.; Wang, H.; Wang, S.; Wang, T. Strong Bulk Photovoltaic Effect in Engineered Edge-Embedded Van Der Waals Structures. *Nat. Commun.* **2023**, *14*, 4230.
(50) Ghosh, S.; Varghese, A.; Thakar, K.; Dhara, S.; Lodha, S. Enhanced Responsivity and Detectivity of Fast WSe_2 Phototransistor Using Electrostatically Tunable in-Plane Lateral Pn Homojunction. *Nat. Commun.* **2021**, *12*, 3336.
(51) Feng, S.; Liu, C.; Zhu, Q.; Su, X.; Qian, W.; Sun, Y.; Wang, C.; Li, B.; Chen, M.; Chen, L. An Ultrasensitive Molybdenum-Based Double-Heterojunction Phototransistor. *Nat. Commun.* **2021**, *12*, 4094.
(52) Zhu, S.; Xie, T.; Lv, Z.; Leng, Y. B.; Zhang, Y. Q.; Xu, R.; Qin, J.; Zhou, Y.; Roy, V. A.; Han, S. T. Hierarchies in Visual Pathway: Functions and Inspired Artificial Vision. *Adv. Mater.* **2024**, *36*, 2301986.
(53) Zhang, G.-X.; Zhang, Z.-C.; Chen, X.-D.; Kang, L.; Li, Y.; Wang, F.-D.; Shi, L.; Shi, K.; Liu, Z.-B.; Tian, J.-G. Broadband Sensory Networks with Locally Stored Responsivities for Neuromorphic Machine Vision. *Sci. Adv.* **2023**, *9*, eadi5104.
(54) Jerry, M.; Chen, P.-Y.; Zhang, J.; Sharma, P.; Ni, K.; Yu, S.; Datta, S. Ferroelectric Fet Analog Synapse for Acceleration of Deep Neural Network Training. In *2017 IEEE international electron devices meeting (IEDM)*, 2017; IEEE: pp 6.2. 1-6.2. 4.
(55) Zhou, Y.; Xu, N.; Gao, B.; Chen, Y.; Dong, B.; Li, Y.; He, Y.; Miao, X. S. Complementary Graphene-Ferroelectric Transistors (C-Gfts) as Synapses with Modulatable Plasticity for Supervised Learning. In *2019 IEEE International Electron Devices Meeting (IEDM)*, 2019; IEEE: pp 6.5. 1-6.5. 4.
(56) Zheng, Y.; Ni, G.-X.; Toh, C.-T.; Tan, C.-Y.; Yao, K.; Özyilmaz, B. Graphene Field-Effect Transistors with Ferroelectric Gating. *Phys. Rev. Lett.* **2010**, *105*, 166602.
(57) Shen, G.; Zhuge, C.; Jiang, J.; Fu, Y.; Zheng, Y.; Qin, Z.; Wang, Q.; He, D. Defective Engineering Tuning the Analog Switching Linearity and Symmetry of Two-Terminal Artificial Synapse for Neuromorphic Systems. *Adv. Funct. Mater.* **2024**, *34*, 2309054.

(58) Zhu, X.; Gao, C.; Ren, Y.; Zhang, X.; Li, E.; Wang, C.; Yang, F.; Wu, J.; Hu, W.; Chen, H. High-Contrast Bidirectional Optoelectronic Synapses Based on 2D Molecular Crystal Heterojunctions for Motion Detection. *Adv. Mater.* **2023**, *35*, 2301468.
(59) Feng, G.; Zhu, Q.; Liu, X.; Chen, L.; Zhao, X.; Liu, J.; Xiong, S.; Shan, K.; Yang, Z.; Bao, Q. A Ferroelectric Fin Diode for Robust Non-Volatile Memory. *Nat. Commun.* **2024**, *15*, 513.
(60) Fuller, E. J.; Gabaly, F. E.; Léonard, F.; Agarwal, S.; Plimpton, S. J.; Jacobs-Gedrim, R. B.; James, C. D.; Marinella, M. J.; Talin, A. A. Li-Ion Synaptic Transistor for Low Power Analog Computing. *Adv. Mater.* **2016**, *29*, 1604310.
(61) Ham, S.; Kang, M.; Jang, S.; Jang, J.; Choi, S.; Kim, T.-W.; Wang, G. One-Dimensional Organic Artificial Multi-Synapses Enabling Electronic Textile Neural Network for Wearable Neuromorphic Applications. *Sci. Adv.* **2020**, *6*, eaba1178.

593 ToC graphic

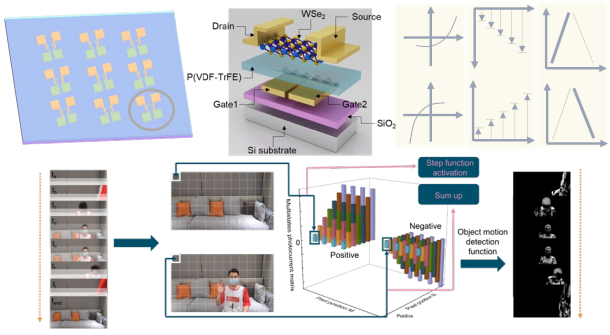

594